

# Optical trapping and binding in air: Imaging and spectroscopic analysis

Marc Guillon<sup>1,\*</sup> and Brian Stout<sup>2</sup>

<sup>1</sup>Laboratoire d'Interférométrie Stellaire et Exoplanétaire, Observatoire de Haute Provence, 04870 Saint Michel l'Observatoire, France

<sup>2</sup>Case 161, Institut Fresnel, Faculté des Sciences et Techniques de St. Jérôme, 13397 Marseille cedex 20, France

(Received 13 October 2007; published 6 February 2008)

We report on an experimental study of direct and spectroscopic imaging of optically trapped Mie droplets in air. The scattering of the trapping beams gives glare points at the droplets' azimuths. Spectroscopic measurements involving polarized light are performed to precisely determine both the droplet sizes and refraction index using Mie scattering theory. Experimental pictures are compared to rigorous numerical simulations. We also include some results on imaging of whispering gallery resonances and conclude with a brief discussion on the possibility of efficiently exciting whispering gallery resonances via radiative coupling.

DOI: [10.1103/PhysRevA.77.023806](https://doi.org/10.1103/PhysRevA.77.023806)

PACS number(s): 42.25.Fx, 42.60.Da, 42.25.Kb

## I. INTRODUCTION

Since the pioneering works on optical forces by Ashkin in the early 1970s [1], and the subsequent general success of optical tweezers, optical trapping has undergone a resurgence of interest with “optical binding” forces [2–4]. Recent works on optical trapping in air have demonstrated the existence of strong longitudinal binding for droplets in the Mie range [5,6]. Quantitative comparison of these results with multiple-scattering theories, however, requires a precise determination of the geometrical and optical properties of the component particles and geometry of the optically bound structures.

In this paper, we propose an experimental spectroimaging setup to accurately determine microdroplet characteristics in the Mie range based on morphology dependant resonances [7,8] and observations of “glare points” [9]. The latter technique has been developed in aerosol science both in the image plane [10] and in the Fourier plane [11] for measurements of droplet sizes and velocities.

In Secs. II–IV we describe the experimental setup and present the basic experimental observations and analysis. We discuss the appearance of glare points occurring both in the scattered trapping light and in spectroscopic measurements manifested as bright dots at the droplet's azimuths. Numerical simulations of the imaging and spectroscopy are compared with observations.

Section V is dedicated to the important role played by the imaging of the highly confined whispering gallery modes (WGM) in the experimental analysis. Inspired by these observations and the fact that these resonances can lead to important increases in the cross sections and radiation pressure [12], we also discuss in this section possible scenarios for efficient radiative couplings to whispering gallery resonances.

## II. EXPERIMENTAL SETUP

The experimental setup includes an imaging system for observing oil and salt-water microdroplets (roughly ranging

from 0.3  $\mu\text{m}$  to 4  $\mu\text{m}$  in radius), suspended in a two-beam optical trap whose geometry is similar to those obtained with optical fibers in water [3,4]. The trapping laser is a 150 mW doubled YAG. The droplets can be trapped for hours thanks to the low values of the vapor pressure and the absorption coefficient of oil and water at the trapping wavelength. The average evaporation rate was measured for oil to be of the order of  $\partial(ka)/\partial t \approx 0.11h^{-1}$  (at 532 nm). This evaporation rate was deduced from the droplet radii and refraction index measurements performed from elastic scattering resonances as discussed in Sec. IV. Although not measured, salt-water droplet evaporation was of the same order of magnitude. We used alimentary sunflower oil for health security and 10 times diluted NaCl-saturated water (at 20 °C) as initially sprayed solutions. A cloud was obtained thanks to a 4 bar air flow in a medical nebulizer and held in a 100 mL syringe before injection in the optical trap.

The light scattered in the 90° direction is imaged with a commercial microscope objective (Melles Griot 0.5 NA,  $\times 25$ ) operating at a standard working distance (1.3 mm). This observation system could be employed thanks to the fact that this optical trap does not require the extremely tight focusing that characterizes conventional optical tweezers [13,14]. The magnification was increased up to 100 thanks to a Barlow lens situated just behind the microscope objective (not shown on Fig. 1). The image was projected on a (3.55 mm  $\times$  2.66 mm, 320 px  $\times$  240 px) CMOS camera.

The optical trapping is achieved with two weakly focused counterpropagating Gaussian beams ( $\approx 1/20$  NA; waist:  $w_0 = 3 \mu\text{m}$ ; Rayleigh distance:  $z_R = 100 \mu\text{m}$ ). The focus of the downward beam is set roughly 300  $\mu\text{m}$  above the upward beam thus yielding a quasiparabolic longitudinal stability [3]. Trap stability in the transverse direction is obtained thanks to the intensity gradient, which pulls the refracting microdroplet toward the strong intensity region. With this configuration, the trapping intensity is  $\approx 3.3 \text{ mW} \cdot \mu\text{m}^{-2}$ . Moreover, since the two ( $\sigma_+$ / $\sigma_-$ ) circularly polarized trapping beams are coherent, they create a fringe pattern onto which the droplet was observed to cling [5], thus freezing the droplet position to sub- $\lambda/2$  precision.

Imaging of the scattered trapping radiation [see Fig. 1(a)] exhibits bright dots which were initially interpreted as two separate droplets [5]. Direct imaging with blue LED light

\*Present address: School of Engineering, Physics and Mathematics, University of Dundee, Dundee, DD1 4HN, U.K. marc.guillon@oamp.fr

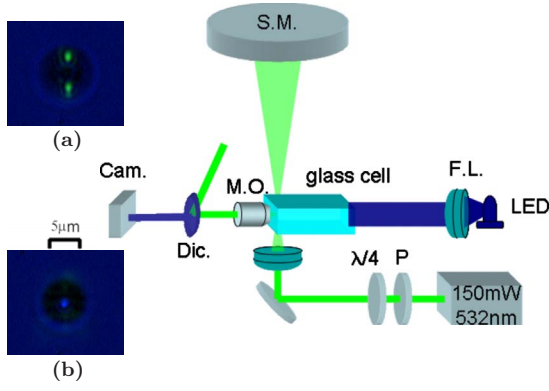


FIG. 1. (Color online) Experimental principle: Oil and salt-water droplets are trapped in two counterpropagating Gaussian beams (150 mW at 532 nm) and illuminated by a blue LED through a field lens (F.L.). Particles are imaged with a 0.5 NA microscope objective (M.O.). A set of dichroic filters (not detailed) allows us to balance the blue and the green light. A polarizer ( $p$ ) and  $\lambda/4$  set was also used to avoid feedback in the laser. The photo in (a) comes from the image formed when the focus of the microscope objective is tuned to the green bright dots (apparently corresponding to the median plane of the droplet) while that in (b) is obtained from the sharpest blue light focus of the droplet. In (b), the bright scattering dots are barely observable in this image since they are now defocused.

emitted along the axis of the microscope objective shows that the two dots arise from the azimuths of a single droplet [15]. An explanation of these bright dots as being a consequence of the excitation of high angular momentum modes in the droplet is developed in the following sections. We also refer the reader to the studies of these “glare points” in aerosol science [9,10] and their occurrence when imaging laser light emitted from microdroplets [16].

### III. PLANE WAVE MODELING

#### A. Validity of the plane wave approximation for numerical simulations

In our experiment, the trapping beams are circularly polarized. This configuration was chosen in order to avoid feedback into the laser using a simple polarizer set. Theoretical calculations predict similar results for the case of linearly polarized beams. Moreover, to achieve the trap stability, the trapping beams are not exactly plane waves, but rather weakly focused Gaussian beams. A theoretical plane wave decomposition of the incident beams is therefore characterized by a relatively narrow angular spectrum. For Gaussian beams, the typical width of the angular spectrum is the focusing angle. The resulting field on the pupil plane of an observing microscope objective can then be interpreted as the superposition of the plane waves in the angular spectrum of the incident field. From a geometrical point of view, summing the scattered fields for different incident plane wave directions is equivalent to fixing the incident angles of the different plane wave components so that they are all oriented along the beam axis and then summing over the scattered

fields throughout the cone corresponding to the relative angles of observation.

For an  $x$ -polarized incident plane wave propagating along the  $z$  axis, the  $\varphi$  dependence of fields  $E_\theta$  and  $E_\varphi$  are  $\cos \varphi$  and  $\sin \varphi$  which corresponds to a narrow spherical wave type image in the direction transverse to beam axis (see the Appendix). The  $\theta$  dependence is more complicated and given by functions  $P_n^1(\cos \theta)/\sin \theta$  and  $\partial P_n^1(\cos \theta)/\partial \theta$ . These functions can be simplified around the  $\theta \sim \pi/2$  direction for  $|\theta - \pi/2| < \pi/2 - 1/n$  at first order in  $1/n$  [17]:

$$\frac{P_n^1(\cos \theta)}{\sin \theta} = \frac{2^{2(n+1)} (n+1)! n! \cos\left[\left(n + \frac{1}{2}\right)\theta + \frac{\pi}{4}\right]}{2^{1/2} \pi (2n+1)! \sin^{3/2} \theta},$$

$$\frac{\partial P_n^1(\cos \theta)}{\partial \theta} = \frac{2^{2(n+1)} (n+1)! n!}{2^{1/2} \pi (2n+1)!} \left[ \frac{2n(n+2) \cos\left[\left(n + \frac{3}{2}\right)\theta + \frac{\pi}{4}\right]}{(2n+3) \sin^{3/2} \theta} - (n+1) \cos \theta \frac{\cos\left[\left(n + \frac{1}{2}\right)\theta + \frac{\pi}{4}\right]}{\sin^{3/2} \theta} \right]. \quad (1)$$

Therefore, as long as the opening angle of the imaging microscope objective is smaller than  $\pi/2 - 1/n_c$  ( $n_c$  being the orbital angular momentum number of the highest excited mode), these developments give a good approximation of the  $\theta$  dependence. The cutoff mode value  $n_c$  is discussed more extensively in the end of Sec. V A.

Inserting the expressions of Eq. (1) into the far field expression given in Eq. (A5) we see that as long as the numerical aperture of the imaging optics is not too large, the angular frequencies of the electric field associated with the excitation of an  $n$  angular quantum number are  $n + \frac{1}{2}$  and  $n + \frac{3}{2}$  in the  $\theta$  coordinate. We can then conclude that the focusing angle of the trapping beams should be inferior to  $\pi/n$  in order to avoid entanglement in the Fourier plane. Since the highest harmonics possibly excited in these microspheres are roughly  $2\pi(Na/\lambda)$  ( $a$  being the radius and  $N \equiv N_{\text{sph}}/N_{\text{med}}$  the index contrast), plane wave simulations should be sufficient to simulate the images generated by  $n$ -order gallery mode excitations provided that the focusing angle of the Gaussian beam satisfies

$$\theta_{\text{foc}} \ll \frac{\lambda}{2Na}. \quad (2)$$

Physically, the limit value corresponds to the angular fringe spacing of the highest whispering gallery mode in the dielectric sphere. Since the waist of a Gaussian beam satisfies  $\lambda/(\pi w_0) \approx \theta_{\text{foc}}$ , the relation in Eq. (2) translates to

$$\pi w_0 \gg 2Na. \quad (3)$$

In our experiment,  $N=1.5$  and the focusing angle is roughly  $1/20$  rad which means that the plane wave imaging approximation should be valid for oil droplet diameters up to  $\sim 7 \mu\text{m}$ .

#### B. Comparison with experimental images

The image obtained both experimentally and theoretically is that of two bright dots at the azimuths of the droplet as

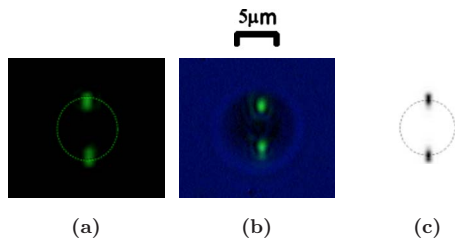


FIG. 2. (Color online) Experimental photos and a simulation for a  $2.70 \mu\text{m}$  radius oil-droplet of refractive index 1.5 trapped in a counterpropagating circularly polarized beam configuration. Picture (a) is taken of the scattered trapping green light only. The circle indicates the perimeter of the sphere as deduced from spectroscopic measurements. In picture (b), imaging blue light incident along the axis of the microscope objective has been added. In (c) we display results from Mie calculations of counterpropagating plane waves followed by Fourier optics simulations of the imaging system (the boundary of the sphere is indicated by a circle).

shown on Fig. 2. A rough physical explanation for the observations of the two dots is that the observed scattered light emanates predominately from the highest excited modes (due in part to the  $2n+1$  factor that appears in Mie calculations of the excitation energy stored in the modes). Furthermore, these high order modes in turn are confined to regions near the surface of the spheres and the emission from the extremities can be understood as “bending losses” of these confined modes. An alternative and complementary explanation has also been presented by Ashkin *et al.* [18] in the context of a ray optics approximation.

In Fig. 2, experimental pictures are compared with a corresponding numerical simulation. The droplet’s radius and index are determined by elastic spectroscopic measurements as described in Sec. IV. Since the intensity of the scattered trapping light is much larger than the imaging blue light, sets of density and dichroic filters are used to reduce the intensity of the bright dots in Fig. 2(b). On this direct imaging picture, the two bright dots appear to be within the perimeter of the droplet contrary to what is obtained both experimentally and theoretically [Figs. 2(a) and 2(c)], where the bright spots appear on the boundary. This phenomenon is apparently principally due to diffraction effects of the direct blue light radiation which slightly enlarge the apparent diameter of the droplet.

### C. Color of the trapping fringe

In the Rayleigh range, optical forces tend to trap dielectric objects with positive refractive index contrast in regions of strong intensity. However, when a dielectric microsphere’s radius becomes comparable to the fringe spacing, the minimum of the trapping “potential” may be centered on a dark fringe, depending on the refractive index contrast and particle size parameter. In a previous article [5], during experimental observations of the interference of the Airy rings, we reported on observing rapid changes in the relative phase of the dot scattering sources emitted from a trapped oil droplet. A likely explanation for this phenomenon now appears that it corresponds to a trapped droplet shifting from being centered

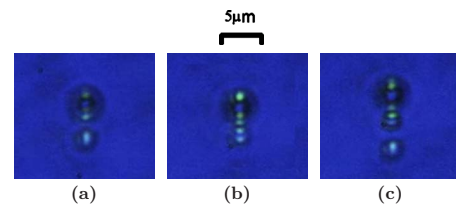


FIG. 3. (Color online) Optically bound salt-water droplets. On each photograph, the largest droplet is roughly  $1.4 \mu\text{m}$  in radius. The smaller droplet radii are approximately  $\pm 25 \text{ nm}$  in (a)  $0.35 \mu\text{m}$ , (b)  $0.45 \mu\text{m}$ , and (c)  $0.45 \mu\text{m}$  (upper) and  $0.35 \mu\text{m}$  (lower). The droplets sizes were deduced from comparison of glare points with numerical simulations.

on a dark fringe to being centered on a bright fringe. Such shifts can be provoked by changes in the droplet’s radius, either due to the slow evaporation process, or by the rapid assimilation of a new droplet from the surrounding cloud. Order of magnitude calculations indicate that capillary deformation under radiation pressure probably does not play a large role in this phenomenon.

Symmetry arguments tell us that only odd modes are excited in a sphere centered on a dark fringe (respectively, even modes for a bright fringe). In the Fourier plane, one can then determine if a microsphere is trapped on a dark or a bright interference fringe by examining the intensity of the central scattered radiation “fringe” in the Fourier plane (cf. Fig. 6).

### D. Mode coupling in optical binding cases

In addition to the commonly observed single trapped droplets, optically bound systems of two or more liquid droplets were also observed. These systems generally involved drops of asymmetric sizes (one relatively large droplet and one or more smaller ones) and could be sufficiently stable (tens of seconds) to allow them to be photographed as illustrated in Fig. 3 for salt-water droplets. Although the size of the large droplets could be determined from spectroscopy measurements, we unfortunately were not able to determine the small droplet size in this manner due to their excessively large free spectral range and the difficulties involved in balancing the scattered intensities emitted from the large and small droplets respectively.

We can see on Fig. 3(a) that very small droplets (radii  $\leq 0.35 \mu\text{m}$ ) exhibit essentially a single glare point. It was generally observed, as illustrated in Fig. 3(b), that the equilibrium separation distance of the surfaces decreases for larger secondary droplets. In Fig. 3(c) two of the droplets are so close they appear to be overlapping (the separation distance diminished when the third droplet arrived). We know, however, that the droplets do not touch in reality since surface tensions would cause them to immediately form a single droplet if they entered into contact. This observation is consistent with our conclusion in the previous section that diffraction effects in the direct microscope imaging of the droplets makes the droplets appear larger than they truly are. Finally, we consistently observed that glare point images were deformed in the optically bound systems [cf. Figs. 3(b)

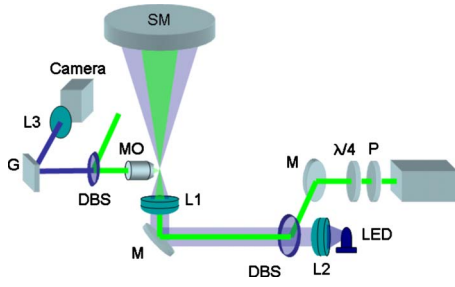


FIG. 4. (Color online) Experimental setup for a spectroscopic determination of droplet properties. The laser is protected with a polarizer set (polarizer  $P$  and  $\lambda/4$ -plate). Blue light coming from a LED is superimposed collinearly thanks to a dichroic beam splitter (DBS) through a field lens ( $L2$ ). The light collected by the microscope objective (MO) is sent onto a blazed grating ( $g$ ) and imaged ( $L3$ ) on a camera. The resulting camera image gives the spectrum along the longitudinal coordinate and the image of the trapping beam axis on the vertical coordinate. The lens ( $L3$ ) is actually a set of two cylindrical lenses, allowing different magnifications along the two transverse directions.

and 3(c)], implying a significant mode coupling of the morphological mode structures.

#### IV. EXPERIMENTAL DETERMINATION OF A DROPLET'S RADIUS AND INDEX

Mie resonances of the optically trapped droplet are determined with a spectroimaging arrangement (shown in Fig. 4) similar to the one previously employed by Chen *et al.* in droplet lasing experiments [16]. In this configuration, a wide spectrum ( $\sim 30$  nm) linearly polarized blue light (centered on 455 nm) illuminates the droplet along the trapping beam axis thanks to a dichroic beam splitter. The light scattered in the  $90^\circ$  direction is collected with a 0.5 NA microscope objective and relayed onto a diffraction grating. The spectrum is observed thanks to a CMOS camera behind a focusing lens as shown in Fig. 5.

The scattered intensity in Fig. 5 exhibits sharp peaks corresponding to Mie resonances in the droplet (either TE or TM depending on the polarization of the incident blue light [18]). At a resonance frequency, the sphere cross section is considerably larger than when it is off resonance. We can see that in the  $90^\circ$  illumination direction, the light always seems to come from the droplets azimuths regardless of a strong excitation of a resonance or not. We conclude that low angular momentum modes, which would give light closer to the center of the droplet, only radiate weakly at these frequencies. Finally, the fact that the entire perimeter of the droplet is not illuminated can be seen as a consequence of the fact that only the  $m=1$  modes are excited by the (nearly) plane wave. The spectra coming from the top and the bottom of the droplet are essentially identical as the optical path in the droplet is the same for both “right” and “left” turning gallery modes.

The precise determination of the droplet's radius and index were obtained by fitting the TE and TM resonant frequencies with Mie scattering theory. In Fig. 5, we illustrate

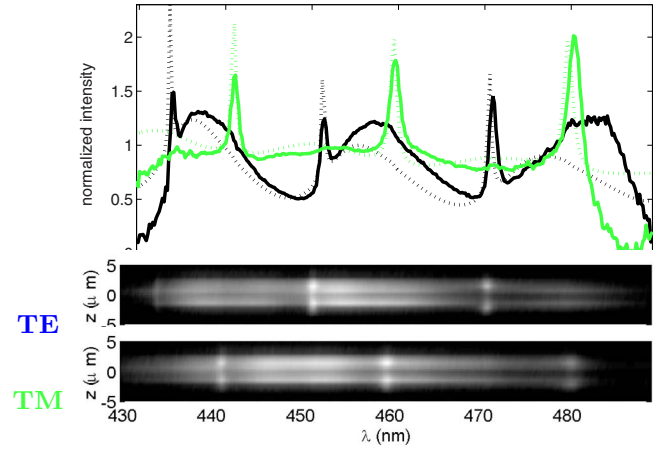


FIG. 5. (Color online) Top figure illustrates the normalized spectra of a trapped oil droplet ( $a=1.29$   $\mu\text{m}$  radius, 1.48 index) illuminated by a polarized wide spectrum blue LED (spectrum centered on 455 nm,  $ka=16.54$ – $18.85$ ). The dotted curves are numerical simulations corresponding to a modeling of the experimental setup of Fig. 4. The two lower pictures correspond to spectral dispersed images for TE ( $n=21, 22, 23$ ) and TM ( $n=20, 21, 22$ ) incident polarizations, respectively. The vertical coordinate is the trapping beam axis and the spectrum is spread over the horizontal (wavelength) coordinate. The bright regions correspond to the “glare points.” The global intensity envelope is that of the illuminating LED source.

normalized experimental spectra fitted with Mie calculations of the near  $90^\circ$  scattered light integrated over the numerical aperture of the microscope objective.

#### V. IMAGE OF RESONATING MODES

##### A. Theoretical image of a single whispering gallery mode (WGM)

In this part, we consider the example of a resonating WGM, described as a resonance of one of the modes  $\mathbf{M}_{omn}$ ,  $\mathbf{M}_{emn}$ ,  $\mathbf{N}_{omn}$ , and  $\mathbf{N}_{emn}$  [19]. In Mie theory, the mode excitation is a function of the size parameter  $ka$  and the dielectric contrast  $N$ , and is determined quantitatively by matching the electric and magnetic field boundary conditions. The field-matching condition depends on the angular momentum number  $n$  and not on its azimuthal quantum number,  $m$ . In the case of TE modes, resonances occur when

$$\frac{[N\rho j_n(N\rho)]'}{j_n(N\rho)} = \frac{[\rho h_n^{(1)}(\rho)]'}{h_n^{(1)}(\rho)} \quad (4)$$

and for TM modes when

$$\frac{[Nj_n(N\rho)]'}{N^2 j_n(N\rho)} = \frac{[\rho h_n^{(1)}(\rho)]'}{h_n^{(1)}(\rho)}, \quad (5)$$

where we recall that  $\rho=ka$ . The conditions in Eqs. (4) and (5) can only be exactly satisfied for a complex wave vector. An imaginary part of the wave vector in a lossless medium corresponds to an imaginary frequency  $\omega$  or, in other words, a field excitation decaying exponentially in time due to radiat-

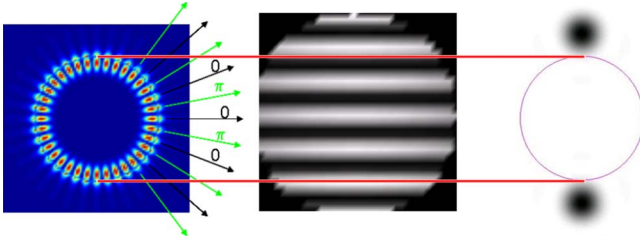


FIG. 6. (Color online) From left to right, near field, pupil plane, and image of a  $(n, n)$  whispering gallery resonance. The far field fringe pattern collected by an imaging lens has the same angular frequency as the near field. In the image plane, the resonance gives two bright dots appearing outside the physical perimeter of the sphere.

ing losses. For highly confined modes, like the WGMs, the imaginary part is small, yielding a long photon lifetime in the cavity.

In the far field limit, only the terms in the  $\mathbf{M}$  and  $\mathbf{N}$  functions proportional to  $e^{ikr}/r$  can be collected by imaging optics. A particularly simple and intriguing case is that of an excited  $m=n$  mode. In this case, the functions  $\mathbf{M}_{onn}$  and  $\mathbf{N}_{enn}$  at infinity are expressed:

$$\begin{aligned} \mathbf{M}_{onn}^{\infty} &= -i^{(n+1)}(2n-1)!! \sin^{n-1}(\theta) \frac{e^{ikr}}{kr} n [\cos(n\varphi) \mathbf{e}_{\theta} \\ &\quad - \sin(n\varphi) \cos(\theta) \mathbf{e}_{\varphi}], \\ \mathbf{N}_{enn}^{\infty} &= i^n (2n-1)!! \sin^{n-1}(\theta) \frac{e^{ikr}}{kr} [n \cos(n\varphi) \cos(\theta) \mathbf{e}_{\theta} \\ &\quad - \sin(n\varphi) \mathbf{e}_{\varphi}]. \end{aligned} \quad (6)$$

Approximating  $\sin^{n-1}(\theta)$  by  $\exp\{-(n-1)[(\theta-\pi/2)^2/2]\}$ , we see that this mode mainly emits near the  $\theta=\pi/2$  plane with a Gaussian type behavior with a divergence angle characterized by  $[1/(n-1)]^{1/2}$ . We also remark that near the  $\theta=\pi/2$  plane the  $\mathbf{M}_{onn}^{\infty}$  and  $\mathbf{N}_{enn}^{\infty}$  far field modes are principally polarized in the  $\mathbf{e}_{\theta}$  and  $\mathbf{e}_{\varphi}$  directions, respectively. The  $\varphi$  dependence is sinusoidal, producing a fringe pattern in the Fourier plane, with angular step equal to  $\pi/n$  (see Fig. 6). The image of this WGM is once again two bright dots, but they are now oriented along the  $\varphi$  direction.

It is worthwhile to remark that despite the fact that near-field interpretations of a WGM indicate energy trapped near the surface of the sphere, far field imaging appears to emanate from sources that appear as located outside of the sphere. Experimental WGM images are more commonly due to light arising from surface Rayleigh scatterers [20,21] and not from intrinsic radiative losses of microresonator due to a finite curvature radius. Such scattering images usually either illuminate the entire perimeter of the microspheres or appear as bright dots on the surface of the microsphere [22]. Images produced by the “bending” losses of the “guided” resonant light are more rare [16] and have different characteristics.

The reason why the sources of the radiated light appear to be located outside the perimeter of the sphere is because the angular quantum numbers  $n$  of the excited resonances are

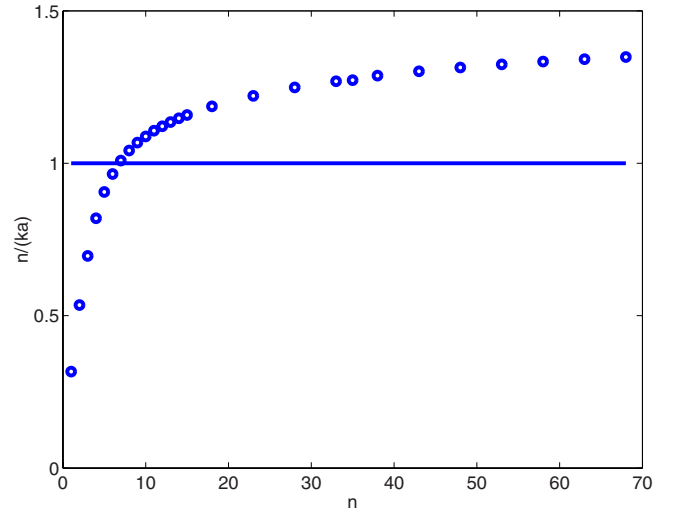


FIG. 7. (Color online) Ratio between the mode numbers of the transverse magnetic resonances and the size parameter at which their sharpest resonance occurs (refractive index contrast of the spheres  $n=1.5$ ). Resonances corresponding to mode numbers higher than 10 will give rise to source regions that will appear to lie outside the physical perimeter since  $n$  in these cases is larger than the size parameter  $ka$  for which they occur.

usually larger than  $ka$  (see Fig. 5, Fig. 7 and [23]). Nevertheless, depending on the sphere size and index contrast, the sharpest excited orbital momentum modes do not necessarily verify  $n > ka$ . For spheres with a refractive index of  $N=1.5$ , we illustrate in Fig. 7 for each magnetic resonance mode number  $n$  the ratio  $n/ka$  where  $ka$  for each  $n$  is the size parameter at which the first (and generally sharpest) resonance for that  $n$  occurs.

We should also remark from the Fig. 7 graph that the ratio  $n/(ka)$  roughly converges toward the refractive index contrast (i.e.,  $N=1.5$  in this case). This value is consistent with the free spectral range in the ray optics approximation when the curvature radius of the sphere becomes large compared with the wavelength. Finally, for large spheres, the sharpest whispering gallery resonance also corresponds to the highest possibly excited mode in the microsphere and drives the cut-off mode value in numerical simulations.

## B. Experimental observations

Examining the spectrally distributed photos in Fig. 5 (the two lower pictures—one for each polarization), we observe two “glare points,” analogous to those described in Sec. II associated with the scattered trapping light. For slightly larger droplets, we could observe four “glare points” [15], two at each azimuth. Furthermore, we observe in Fig. 8 that resonances appear at slightly different positions along the trapping beam axis as functions of their “angular quantum number” (even if the spectrometer barely resolves the sharpest resonances). In Fig. 8, TE resonances appear as sharp lines outside the droplets’ perimeter (more visible on the logarithmic scale). Gallery resonances appear as vertical lines and not dots as numerically modeled in Fig. 6 because

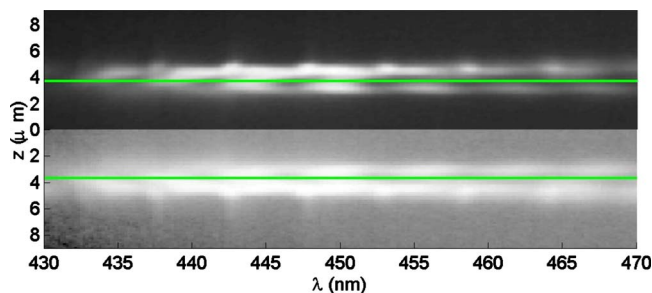


FIG. 8. (Color online) Spectrally dispersed upper glare point of a  $3.66 \mu\text{m}$  radius oil-droplet with TE-polarized illuminating light. The droplet's center is adopted as the origin of the axial coordinates,  $z=0$ . The lower graph is a horizontal mirror of the top picture using a logarithmic scale in intensity. The physical position of the droplet perimeter is indicated by the (green) lines. The images of the sharp gallery resonances (more readily visible on the logarithmic scale) appear as if located outside of the physical droplet perimeter.

of different experimental imaging powers for the horizontal (spectrum) and vertical coordinates by means of a set of cylindrical lens (replacing  $L3$  in Fig. 4). Therefore, the image is lengthened along the vertical coordinate.

A full vertical resolution of all the modes would require a 1(NA) imaging system. The less confined excited modes interfere in the image plan and yield the large spots appearing close to the physical perimeter. One can also observe that the bright regions appearing at distances lying within the physical droplet perimeter have a much broader resonance spectra.

### C. Radiative coupling

These observations of radiating characteristics may prove useful in understanding and optimizing radiative couplings with dielectric (i.e., “open”) microcavities. According to the reciprocity principle [24], if an outgoing Mie radiation mode [like that described in Eq. (6)] yields a Gaussian type radiation pattern in the image plane of a microscope objective, it should then be proved possible to radiatively couple a Gaussian beam to this highly confined resonance. The coupling efficiency would then chiefly depend on the numerical aperture of the imaging system. As previously numerically shown [25], the optimum coupling efficiency is obtained by focusing the Gaussian beam outside the physical perimeter of the microsphere. We argue a  $\sim 30\%$  coupling efficiency could be obtained thanks to a standard 0.75 NA microscope objective by using a beam with two different waists. According to the far field given by an  $(n, n)$  mode [given in Eqs. (6)], an optimized coupling beam should have the following characteristics:

$$\begin{aligned} kw_z &= 2(n-1)^{1/2}, \\ kd &\approx Nka, \end{aligned} \quad (7)$$

where  $w_z$  is a Gaussian formed beam waist along one transverse ( $z$ ) coordinate,  $n$  is the resonance mode number, and  $d$  is the optimum impact parameter, given as a function of the

sphere radius  $a$  and the index contrast  $N$ . For an optimized coupling, the beam profile along the other coordinate should be an Airy spot as small as possible. This argument is not very intuitive since the smaller the focus spot, the smaller the overlap with the sphere in the waist plane. On the other hand, the smaller the beam size, the larger the divergence angle. Thus the beam turns around the sphere, increasing the optical path along both the sphere and the coupling length.

## VI. CONCLUSION

We observed  $90^\circ$  elastic light scattering from oil microdroplets in the Mie range. The image given by the microscope objective was compared to numerical simulations. The radius of the droplet was obtained by fitting whispering gallery resonances with Mie-scattering-theory modeling of our experimental setup. We also showed that the precise form of the glare points depends on the angular momentum number of the excited resonant modes. Beyond the intrinsic value of this type of analysis to studies of multiple-particle trapping and binding, this study may also prove useful in studies of morphological mode couplings and radiation and radiative excitations of whispering gallery modes. A possible application to the optimization of radiative couplings to spherical microcavities was given in this regard. Optimized radiative coupling may offer an interesting alternative to fiber taper [26] and prism [27] couplings. From this perspective, optical trapping of the microparticles appears as a rather promising tool in isolating these cavities from their environment.

## ACKNOWLEDGMENTS

The authors are grateful to J. P. Reid and A. Labeyrie for helpful discussions and encouragement.

## APPENDIX: MIE THEORY MODELING OF THE FIELD COLLECTED BY A MICROSCOPE OBJECTIVE

Scattering of a plane wave by a spherical particle is given by Mie theory. This approximation is sufficient in our case to describe the scattered trapping light due to the relatively modest value of the numerical aperture involved in the trapping beam focus. We discuss this point more extensively in Sec. III A. More precise calculations could be performed by projecting the Gaussian beams onto the vector spherical wave basis [28].

An  $x$ -polarized plane wave propagating along the  $z$  axis can be easily split into spherical harmonics and can be written thanks to functions  $M_{o1n}$  and  $N_{e1n}$  [19]:

$$\mathbf{E}_i = E_0 \sum_{n=1}^{\infty} i^n \frac{2n+1}{n(n+1)} (\mathbf{M}_{o1n}^{(1)} - i\mathbf{N}_{e1n}^{(1)}), \quad (\text{A1})$$

where the superscript is for a radial dependence given by spherical Bessel functions of the first kind. The scattered electric field is developed as

$$\mathbf{E}_s = E_0 \sum_{n=1}^{\infty} i^n \frac{2n+1}{n(n+1)} (-b_n \mathbf{M}_{o1n}^{(3)} + ia_n \mathbf{N}_{e1n}^{(3)}), \quad (\text{A2})$$

where the Mie coefficients  $a_n$  and  $b_n$  are determined by matching spherical wave boundary conditions. In the ab-

sence of scattering objects in the beams, the field collected by the microscope objective is essentially zero. Consequently, the image modeling must only take the scattered field into account. Its radial dependence is given by spherical Hankel functions of the first kind [29].

In the pupil plane of the microscope objective, only the  $1/r$  term of the development is kept. At infinity,  $h_n^{(1)}$  becomes

$$\lim_{\rho \rightarrow \infty} h_n^{(1)}(\rho) \sim i^{-(n+1)} \frac{e^{i\rho}}{\rho}, \quad (\text{A3})$$

which yields simplified expressions for the  $\mathbf{M}_{omn}$  and  $\mathbf{N}_{emn}$  functions at infinity:

$$\begin{aligned} \mathbf{M}_{omn}^{\infty} &= \left[ m \cos m\varphi \frac{P_n^m(\cos \theta)}{\sin \theta} \mathbf{e}_{\theta} \right. \\ &\quad \left. - \sin m\varphi \frac{dP_n^m(\cos \theta)}{d\theta} \mathbf{e}_{\varphi} \right] i^{-(n+1)} \frac{e^{ikr}}{kr}, \\ \mathbf{N}_{emn}^{\infty} &= \left[ \cos m\varphi \frac{dP_n^m(\cos \theta)}{d\theta} \mathbf{e}_{\theta} \right. \\ &\quad \left. - m \sin m\varphi \frac{P_n^m(\cos \theta)}{\sin \theta} \mathbf{e}_{\varphi} \right] i^{-n} \frac{e^{ikr}}{kr}. \end{aligned} \quad (\text{A4})$$

Axially oriented incident plane waves are composed uniquely of  $m=1$  components and, since the Mie coefficients are diagonal in both angular and azimuthal quantum numbers, the scattered electric field is likewise composed uniquely of  $m=1$  coefficients which yields for the electric field of the scattered wave

$$\mathbf{E}_r = O\left(\frac{1}{(kr)^2}\right),$$

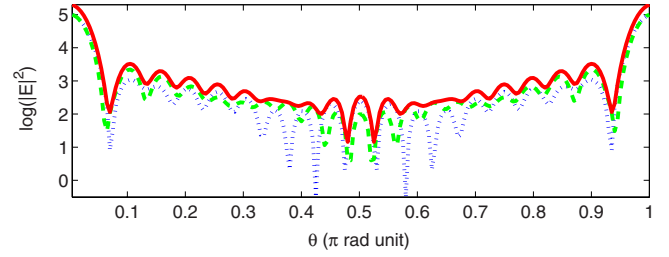


FIG. 9. (Color online) Far field scattering from counterpropagating plane waves impinging on a spherical dielectric sphere (index 1.5,  $ka=23$ ) as a function of  $\theta$ . Blue dotted curve:  $\mathbf{e}_{\theta}$  polarized field; green dashed curve:  $\mathbf{e}_{\varphi}$  polarized field; red solid curve: total intensity. The energy scattered in the  $90^{\circ}$  direction is roughly one hundred times as small as in the forward direction.

$$\begin{aligned} \mathbf{E}_{\theta} &= iE_0 \cos \varphi \frac{e^{ikr}}{kr} \sum_{n=1}^{\infty} \frac{2n+1}{n(n+1)} \left[ a_n \frac{\partial P_n^1(\cos \theta)}{\partial \theta} \right. \\ &\quad \left. + b_n \frac{P_n^1(\cos \theta)}{\sin \theta} \right], \\ \mathbf{E}_{\varphi} &= -iE_0 \sin \varphi \frac{e^{ikr}}{kr} \sum_{n=1}^{\infty} \frac{2n+1}{n(n+1)} \left[ a_n \frac{P_n^1(\cos \theta)}{\sin \theta} \right. \\ &\quad \left. + b_n \frac{\partial P_n^1(\cos \theta)}{\partial \theta} \right]. \end{aligned} \quad (\text{A5})$$

In the case of large spheres, a plane wave is predominately scattered in the forward direction(s). The light scattered in the  $90^{\circ}$  direction is only a small energy fraction of the total scattered radiation as can be seen in Fig. 9.

The two bright dots which can be seen on the picture of Fig. 1 can roughly be interpreted as the Fourier transform of the electric field close to  $\pi/2$ . In Fig. 9, we see that the scattered electric field oscillates rapidly in this region, qualitatively corroborating experimental observations.

- 
- [1] A. Ashkin, Phys. Rev. Lett. **24**, 156 (1970).  
[2] M. M. Burns, J.-M. Fournier, and J. A. Golovchenko, Phys. Rev. Lett. **63**, 1233 (1989).  
[3] S. A. Tatarkova, A. E. Carruthers, and K. Dholakia, Phys. Rev. Lett. **89**, 283901 (2002).  
[4] W. Singer, M. Frick, S. Bernet, and M. Ritsch-Marte, J. Opt. Soc. Am. B **20**, 1568 (2003).  
[5] M. Guillon, O. Moine, and B. Stout, Phys. Rev. Lett. **96**, 143902 (2006).  
[6] M. Guillon, Proc. SPIE **6483**, 648302 (2007).  
[7] H. Tzeng, K. Wall, M. Long, and R. Chang, Opt. Lett. **9**, 499 (1984).  
[8] H. Tzeng, K. Wall, M. Long, and R. Chang, Opt. Lett. **9**, 273 (1984).  
[9] H. V. de Hulst and R. Wang, Appl. Opt. **30**, 4755 (1991).  
[10] Y. Zama, M. Kawahashi, and H. Hirahara, Opt. Rev. **11**, 358 (2004).  
[11] N. Damaschke, H. Nobach, T. Nonn, N. Semidetnov, and C. Tropea, Exp. Fluids **39**, 336 (2005).  
[12] A. Ashkin and J. Dziedzic, Appl. Opt. **19**, 660 (1980).  
[13] A. Ashkin, J. Dziedzic, J. Bjorkholm, and S. Chu, Opt. Lett. **11**, 288 (1986).  
[14] R. Omori, T. Kobayashi, and A. Suzuki, Opt. Lett. **22**, 816 (1997).  
[15] M. Guillon, O. Moine, and B. Stout, Phys. Rev. Lett. **99**, 079901(E) (2007).  
[16] G. Chen, M. Mazumder, Y. Chemla, A. Serpengüzel, R. Chang, and S. Hill, Opt. Lett. **18**, 1993 (1993).  
[17] I. Gradshteyn and I. Ryzhik, in *Table of Integrals, Series and Products*, 6th ed., edited by A. Jeffrey and D. Zwillinger (Academic, New York, 2000).  
[18] A. Ashkin and J. Dziedzic, Appl. Opt. **20**, 1803 (1981).  
[19] C. Bohren and D. Huffman, *Absorption and Scattering of Light by Small Particles* (Wiley-Interscience, New York, 1983).

- [20] M. Cai and K. Vahala, *Opt. Lett.* **26**, 884 (2001).
- [21] L. Yang and K. Vahala, *Opt. Lett.* **28**, 592 (2003).
- [22] Y.-S. Choi, H.-J. Moon, S. Kim, and K. An, e-print arXiv:physics/0106032.
- [23] P. Chylek, V. Ramaswamy, A. Ashkin, and J. Dziedzic, *Appl. Opt.* **22**, 2302 (1983).
- [24] L. Landau, E. Lifshitz, and L. Pitaevskii, *Electrodynamics of Continuous Media*, 2nd ed. (Elsevier Butterworth-Heinemann, Oxford, 2006).
- [25] E. Khaled, S. Hill, P. Barber, and D. Chowdhury, *Appl. Opt.* **31**, 1166 (1992).
- [26] J. Knight, G. Cheung, F. Jacques, and T. Birks, *Opt. Lett.* **22**, 1129 (1997).
- [27] M. Gorodetsky and V. Ilchenko, *J. Opt. Soc. Am. B* **16**, 147 (1999).
- [28] O. Moine and B. Stout, *J. Opt. Soc. Am. B* **22**, 1620 (2005).
- [29] I. Gradshteyn and I. Ryzhik, in *Table of Integrals, Series and Products*, 6th ed., edited by A. Jeffrey and D. Zwillinger (Ref. [17]).